Quasiparticle Spectroscopy, Transport, and Magnetic Properties of Nb Films Used in Superconducting Qubits

Kamal R. Joshi[1], Sunil Ghimire[1,2], Makariy A. Tanatar[1,2], Amlan Datta[1,2], Jin-Su Oh[1],
Lin Zhou[1], Cameron J. Kopas[3], Jayss Marshall[3], Josh Y. Mutus[3], Julie Slaughter[1],
Matthew J. Kramer[1], James A. Sauls[4] and Ruslan Prozorov[1,2,*]

[1]*Ames National Laboratory, Ames, Iowa 50011, USA*

[2]*Department of Physics & Astronomy, Iowa State University, Ames, Iowa 50011, USA*

[3]*Rigetti Computing, 775 Heinz Avenue, Berkeley, California 94710, USA*

[4]*Hearne Institute of Theoretical Physics, Department of Physics & Astronomy, Louisiana State University, Baton Rouge, Louisiana 70803, USA*

Niobium thin films on silicon substrate used in the fabrication of superconducting qubits have been characterized using scanning and transmission electron microscopy, electrical transport, magnetization, the London penetration depth - based quasiparticle spectroscopy, and real-space real-time magneto-optical imaging. We study niobium films to provide an example of a comprehensive analytical set that may benefit superconducting circuits such as those used in quantum computers. The films have a superconducting transition temperature of $T_c = 9.35$ K and a fairly clean superconducting gap. The estimated superfluid density is enhanced at intermediate temperatures. These observations are consistent with the recent theory of anisotropic strong-coupling superconductivity in Nb and indicate outstanding quality. However, the response to the magnetic field is complicated, exhibiting significantly irreversible behavior and insufficient heat dissipation (to a substrate), leading to thermomagnetic instabilities. This may present a challenge for further improvement of transmon quantum coherence. Possible mitigation strategies are discussed.

I. INTRODUCTION

Superconducting qubits are promising candidates for implementing large-scale quantum computers [1–3]. The advancement in fabrication and design of superconducting qubits has demonstrated impressive gate fidelity of up to 99.5% for two-qubit gates, which is the measure of the ability of a device to faithfully execute quantum algorithms [4]. However, large-scale devices will require fidelity well beyond 99.9% [5]. It has been shown that certain impurities and defects in qubit material tend to shorten the coherence time and lead to overall lower-fidelity operations [6–8]. For example, microwave loss at cryogenic temperatures has been attributed to the resonant coupling to two-level systems (TLSs) physically composed of the atomic defects [7,9]. Therefore, achieving better fidelities requires improved quantum coherence and that necessitates a better understanding and control over the materials used to fabricate qubits.

Niobium is the material of choice for various superconducting applications due to its relatively high transition temperature, $T_c = 9.35$ K. Niobium thin films (100–200 nm thick) are widely used in superconducting transmon qubits [1]. The "heart" of such qubits is an aluminum Josephson junction used to provide nonlinearity to the circuit and niobium leads occupy practically the entire volume of the circuit: the readout resonators, capacitor pads, and coupling lines in the transmon. In order to work, the structure must have a high degree of quantum coherence in all parts. Surfaces and interfaces are known to introduce noise and loss that play a major role in decreasing the coherence time in transmon qubits [7,10–13]. For instance, the native amorphous oxides with different stoichiometry (NbO, NbO_2, and Nb_2O_5) that are present are believed to be the host for TLSs; hence the decoherence [14–17]. Another recently discovered source of potential decoherence in transmons is nanosized niobium hydrides [7]. Large hydrides in the superconducting rf cavities are believed to be the cause of the so-called Q disease (a dramatic reduction of the quality factor above some amplitude of the electromagnetic field inside the cavity) and have been known for a long time [18–23]. While bulk niobium used in superconducting-radio-frequency (srf) cavities has been extensively characterized in both the normal and the superconducting state, the niobium films used in quantum information science (QIS) technologies have mostly

*Corresponding author. prozorov@ameslab.gov

024031-1

been studied to examine the quality-factor behavior and losses at gigahertz frequencies [24]. Bulk and films of niobium are very different [25,26] in terms of morphology, purity, and relative length scales involved and more conventional studies in the superconducting state are needed. An important aspect is the application mode, which is usually at a radio frequency of a few gigahertz [27], whereas characterization is often performed at lower frequencies [28,29]. In general, niobium films for use in superconducting qubits is an active area of research (see, e.g., Ref. [30] and references therein).

In this work, we employ various techniques to study thermally excited quasiparticles, electrical transport, upper and third critical fields, magnetization, and spatial distribution of the magnetic induction in niobium thin films and suggest strategies for further material optimizations and improvements.

II. EXPERIMENTAL

Niobium films, 160 nm thick, were deposited onto [001] high-resistivity silicon wafers ($> 10\,000\ \Omega$ cm) using high-power impulse magnetron sputtering (HiPIMS) in an ultrahigh-vacuum system with a base pressure $< 1 \times 10^{-8}$ Torr [8,31,32].

The film morphology was studied using scanning electron microscopy (SEM), including high-resolution SEM, and transmission electron microscopy (TEM). A more detailed investigation of transmons using Nb from the same batch as in this work, and imaging details, are available elsewhere [33]. Cross-section and plan-view TEM samples were prepared with a Helios focused-ion-beam (FIB) system. The TEM images were acquired at an acceleration voltage of 200 kV using a Titan Themis. SEM was used to map out the larger view of the sample-surface morphology. The TEM images were used for quantitative analysis.

Quasiparticles are known to be one of the major sources of decoherence in superconducting qubits [34, 35]. The density of the quasiparticles is proportional to $\sqrt{\pi \Delta(0)/2k_B T} \exp(-\Delta(0)/k_B T)$, which is proportional to $\Delta\lambda(T)$. To study the low-energy quasiparticles, we used a tunnel-diode resonator (TDR) for the precision measurements of the London penetration depth, $\Delta\lambda(T)$ [36,37], which was then used to calculate the superfluid density, $\rho(T) = 1/(1 + \Delta\lambda(T)/\lambda(0))^2$, which may be compared to the expectations from the theory. Here, the zero-temperature value of the penetration depth, $\lambda(T = 0) \approx 33$ nm, was estimated for niobium film identical to that used in our earlier work [38]. The measurement technique uses a self-oscillating TDR, described in detail elsewhere [36,37,39–41]. Briefly, the highly stable TDR circuit resonates at approximately 14 MHz and the frequency shift is measured with a precision better than 1 ppb (part per

billion). The inductor coil generates an ac-excitation magnetic field, $H_{ac} < 20$ mOe; hence the sample is always in the Meissner state at the temperatures of interest. In the experiment, the sample is mounted on a 1-mm-diameter sapphire rod and inserted into a 2-mm-diameter inductor coil. The coil and the sample are situated in a vacuum inside a ^{3}He cryostat or a dilution refrigerator. The TDR circuit is actively stabilized at 5 K by a LakeShore temperature controller and the sample is controlled separately from 350 mK by an independent LakeShore controller. The change of the resonant frequency when a sample is inserted into the coil is proportional to the sample magnetic susceptibility as long as the change of the total inductance is small and one can expand $\Delta f/f_0 \approx \Delta L/2L_0$, where $2\pi f_0 = 1/\sqrt{CL_0}$, in which the subscript zero refers to an empty resonator. The coefficient of proportionality, which includes the demagnetization correction, is measured directly by pulling the sample out of the resonator at the base temperature [40–42]. A general analysis of the calibration procedure for nonellipsoidal samples is given elsewhere [42].

It must be noted that perhaps a more familiar experimental technique used to measure the London penetration depth with a precision sufficient to discuss the superconducting-gap structure—and hence thermal quasiparticles—is the microwave-cavity perturbation technique [43,44]. The physics is similar to that of TDR: a sample is placed inside the microwave cavity on a temperature-controlled holder (usually sapphire). The cavity is constructed so that the sample only "sees" the magnetic component of an ac field. Any change in the magnetic susceptibility of the sample results in a change in the resonant peak frequency and shape. In fact, this was the first technique that unequivocally showed a nodal superconducting gap consistent with a *d*-wave pairing in hole-doped cuprate high-T_c superconductor Y-Ba-Cu-O [43]. Compared to TDR, the microwave-cavity setup is much bulkier; has more complicated electronics; does not allow the application of an external magnetic field (the cavity must be superconducting to maintain a high quality factor, Q); has a much larger amplitude of the excitation magnetic field acting on the sample; has lower resolution; and is much slower and hence prone to signal drift in time. There have been significant improvements of this technique. The breakthrough came with the introduction of rutile (TiO$_2$)—a dielectric material with a high dielectric constant, $\epsilon = 120$, and a low loss tangent, $\tan\delta = 3 \times 10^{-8}$ [45,46]. The new generation of rutile-based microwave resonators is much more compact and allows the application of high magnetic fields. The advantage of the microwave perturbation technique, compared to TDR, is that it provides both components of the response by measuring not only the resonant frequency shift but also the change in the quality factor. This gives direct access to the absolute value of the London penetration depth, $\lambda(0)$

[44,47]. Another advantage is that it operates at the frequencies of superconducting transmon qubits. Therefore, the dissipation that it finds is directly related not only to static but also dynamic pair breakers such as TLSs that presumably limit transmon quantum coherence at low temperatures.

Four-probe electrical resistivity measurements were performed in a Quantum Design physical property measurement system (PPMS). Contacts were made by gluing 25-μm silver wires using DuPont 4929N conducting silver paste. This technique yields contacts with contact resistance in the (10–100)-Ω range. Transport measurements of the upper critical field, H_{c2}, were performed with a magnetic field oriented perpendicular to the film plane to avoid the third critical field, H_{c3}, which does not exist in this orientation but is a maximum when the magnetic field is parallel to the film surface [48,49]. For measurements in a parallel configuration, the sample was glued on the side of the plastic cube, similar to those described in Ref. [50]. This procedure provided alignment with the accuracy of about $2°$.

Total magnetization was measured using a vibrating sample magnetometer (VSM) module in the Quantum Design PPMS. The advantage of this device is the ability to sweep the magnetic field continuously at a constant rate.

The two-dimensional distribution of the magnetic induction was mapped in real time employing magneto-optical imaging using the Faraday effect (MOFA) in transparent ferrimagnetic indicators (bismuth-doped iron garnets) placed on top of the samples. The closed-cycle flow-type optical ^{4}He cryostat exposed the cooled sample to an Olympus polarized-light microscope. The magnetic induction on the sample surface polarizes in-plane magnetic moments in the indicator and the distribution of this polarization component along the light propagation is visualized through double Faraday rotation. In the images, only the magnetic field is visible due to a mirror sputtered at the bottom of the indicator [51–54].

III. RESULTS

Figure 1 shows the morphology of the Nb film revealed by high-resolution scanning electron microscopy (HR SEM) and TEM. Figure 1(a) shows the SEM image of a wide view of the top-surface morphology, revealing substantial spatial modulations at two characteristic length scales. Further details of the internal and surface structural texture are revealed by the bright-field plan-view TEM image [Fig. 1(b)] and a cross-section view [Fig. 1(c)]. The contrast variation reveals a granular polycrystalline structure on top of and inside the film. Based on the statistics from more than 100 grains, their sizes range from 30 nm to 90 nm, with an average size of about 60 nm. Those
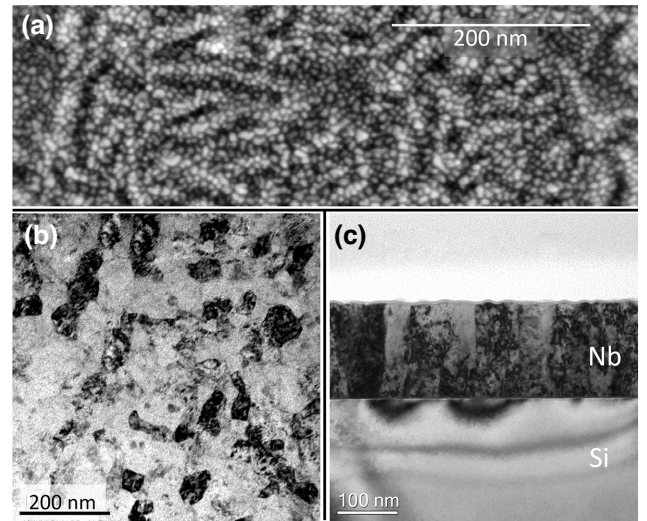

FIG. 1. (a) The wide-area view of the sample surface morphology revealed by high resolution SEM of the sample-surface morphology. (b),(c) The TEM plan view (b) and TEM cross-section view (c) of the studied Nb thin film. The bulk consists of columnar Nb grains with a fairly broad distribution of sizes ranging between 30 and 90 nm, with an average grain size of about 60 nm. The surface roughness is of the order of 3–5 nm.

grains have a columnar structure along the film thickness, measured at 160 nm as intended by the fabrication. The smaller droplets observed in secondary-electron image contrast [Fig. 1(a)] represent the surface roughness, which is also seen in the cross-section view [Fig. 1(c)].

Figure 2 presents electrical-resistance measurements as a function of the magnetic field and the temperature. The data were collected in parallel and perpendicular orientations of the film with respect to the applied magnetic field. In a parallel orientation, the material remains superconducting up to a so-called third critical magnetic field, H_{c3}, surviving in a thin surface layer of the order of the superconducting coherence length, ξ [48,49,55]. In niobium, $\xi \approx 10 - 40$ nm, depending on its purity and degree of crystallinity [48,56–58]. In the perpendicular orientation of the magnetic field to the film plane, the upper critical field, H_{c2}, is the highest magnetic field possible [48,49,59]. Therefore, we obtain these two critical magnetic fields from the measurements of the same sample by simply rotating it through $90°$ without changing the contacts. In the PPMS, the cooling is achieved via the helium exchange gas when the sample is mounted on a puck and so the orientation is not important for thermal equilibrium as long as the measurements are performed slowly. Indeed, we see the same $T_c = 9.35$ K in zero magnetic fields in both orientations.

Figure 2(a) (left) shows the magnetic-field-dependent resistance, $R(H)$, measured at different temperatures from 2 to 8 K in 1 K steps. Figure 2(a) (right) shows the
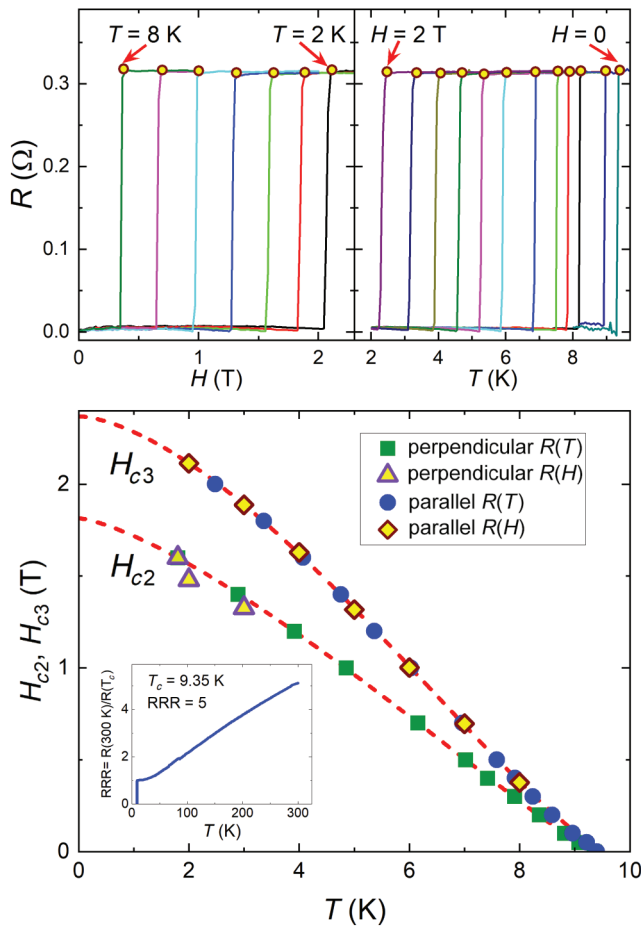
FIG. 2.   (a) The electrical resistance of Nb film in a magnetic field parallel to the film plane. Left, $R(H)$ scans measured at different temperatures from 2 to 8 K at 1 K intervals. Right, $R(T)$ scans at fixed magnetic fields, from right to left: $H = 0$, 0.1, 0.3, 0.4, 0.5, 0.7, 1.0, 1.2, 1.4, 1.6, 1.8 and 2 T. (b) The summary phase diagram, showing the third critical field, H_{c3}, obtained from the data shown in (a), and the upper critical field, H_{c2}, obtained from similar measurements with the magnetic field oriented perpendicular to the plane. The inset shows the temperature-dependent resistivity normalized by its value at T_c. $RRR = R(300\,\text{K})/R(T_c) = 5$.

temperature-dependent resistance, $R(T)$, measured at different magnetic fields, from right to left: $H = 0$, 0.1, 0.3, 0.4, 0.5, 0.7, 1.0, 1.2, 1.4, 1.6, 1.8, and 2 T. In both panels of Fig. 2(a), the symbols show the locations of the third critical field, $H_{c3}(T)$ (left panel) or the critical temperatures, $T_c(H_{c3})$ (right panel), an easy pick, considering how sharp the transitions remain for all curves. Similar measurements were performed in the perpendicular orientation, yielding the upper critical field, $H_{c2}(T)$. Figure 2(b) summarizes the results of the critical-field measurements. The upper curve, obtained from the data in Fig. 2(a), shows the third critical field, $H_{c3}(T)$. The agreement between

the two types of scans is outstanding. Similarly, the lower curve shows the upper critical field, $H_{c2}(T)$.

The inset shows temperature-dependent resistivity normalized by its value at T_c in a broad temperature range up to 300 K. At 300 K, this ratio, called the residual resistivity ratio, $RRR(300\,\text{K}) \approx 5$, is the commonly used measure of scattering on defects and impurities. For comparison, the cleanest niobium samples reach $RRR = 90\,000$ [60] and so the value of 5 for our films is rather low.

We now examine the superconducting state of the studied films. Figure 3 shows the temperature-dependent superfluid density, $\rho(T) = \lambda^2(0)/\lambda^2(T)$, obtained from the London penetration depth, $\lambda(T)$, measured using a TDR [36,37]. The solid red curve is the expectation from the isotropic weak-coupling Bardeen-Cooper-Schrieffer (BCS) theory [61]. This measurement is quite difficult due to the extreme thin-film geometry. The upper inset in Fig. 3 shows the full transition curve, which looks flawless but cuts off at about $\Delta\lambda(T_{\text{cm}}) = 3.3\,\mu\text{m}$, at which point the film becomes transparent to our 10-MHz rf field. This formally follows from the analysis of the magnetic susceptibility in finite samples [42]. For our films, the formal calibration gives for the effective sample size $R = 3\,\mu\text{m}$, which matches the above experimental value for the penetration depth at T_c perfectly when the response becomes "sample size limited" [42]. This also explains why the measured transition temperature from the penetration-depth measurement, $T_{\text{cm}} = 9.03$ K, is a little lower than the $T_c = 9.35$ K detected by the transport measurements [see Fig. 2]. The lower inset is an enlargement of the lower-temperature behavior. Remarkably, the penetration depth changes only by 10 nm from the base temperature up to $0.8\,T_c$ and yet we were able to resolve the whole superfluid density curve shown in Fig. 3. A clear exponential saturation at low temperatures signals a full superconducting gap. If we fit the data to a low-temperature BCS formula, valid below $0.3\,T_c$, $\Delta\lambda/\lambda(0) = \sqrt{\pi\delta/2t}\exp(-\delta/t)$ [37], where $\delta = \Delta(0)/k_B T_c$ and $t = T/T_c$, and use δ as a free parameter, we obtain $\delta \approx 1.3$ instead of the isotropic BCS value of $\delta \approx 1.76$. This is most likely associated with the electronic and superconducting states anisotropy of niobium and its multiband nature [58]. In this situation, the range of exponential attenuation is determined by the smaller gap, specifically on band 2, which also dominates the thermodynamic response [58]. The theory is further confirmed by the observed deviation of the experimental superfluid density at elevated temperatures from the weak-coupling expectation, shown by the solid red line in Fig. 3. Stronger coupling makes $\rho(T)$ lie above the weak-coupling values [58]. In principle, precision measurements of the London penetration depth as function of the temperature provide superconducting-gap spectroscopy mapping out the density of states of thermally excited quasiparticles. Mechanisms leading to pair breaking—e.g., spin-flip scattering on magnetic impurities—lead to
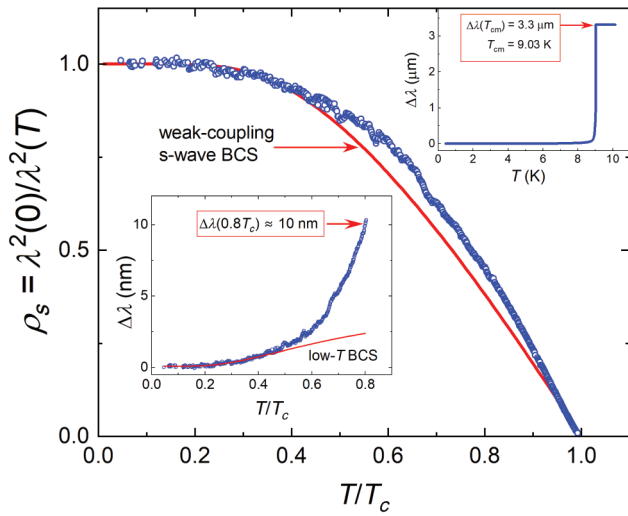
FIG. 3. The normalized superfluid density evaluated from the measured London penetration depth shown in the insets using the formula shown in the vertical-axis title. The solid red curve is the expectation from the isotropic weak-coupling BCS theory [61]. The upper inset shows a full-temperature range variation, whereas the lower-left inset shows the data up to $0.8T_c$. The red line is a fit to the isotropic low-temperature asymptotic BCS formula described in the text. Note very small total variation of $\Delta\lambda(T)$, due to the significantly reduced effective sample dimension as a result of the thin-film geometry [42].
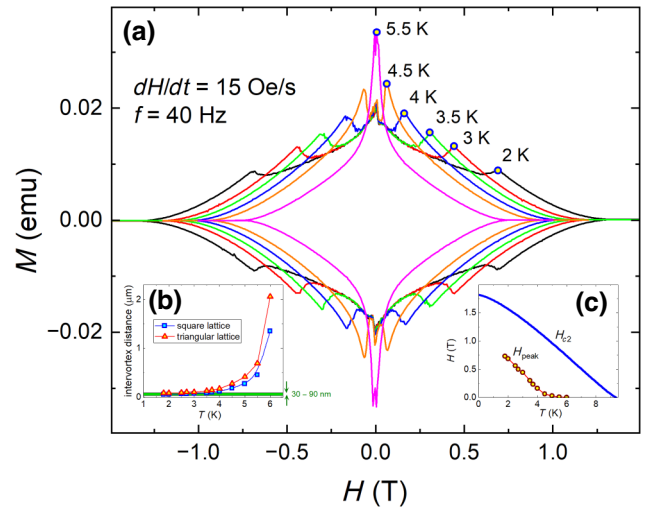

FIG. 4. (a) The VSM measurements of the hysteresis $M(H)$ (magnetization versus applied field) loops at indicated temperatures. There is a peaklike feature at the intermediate fields, marked by open circles, that shifts to the lower fields at higher temperatures. (b) The intervortex distance for square- and triangular-vortex lattices calculated from the peak positions. This distance is of the order of the morphological features from the TEM images (Fig. 1) from 30 to 90 nm, making it plausible that very similar physics is involved. (c) The peak feature on the H-T phase diagram, plotted along with the upper critical field, $H_{c2}(T)$.

the reduction of T_c [62] and significant modification of $\lambda(T)$ [63].

Figure 4 shows profound features on the $M(H)$ magnetic hysteresis loops obtained using the Quantum Design PPMS vibrating sample magnetometer (VSM) operating at a frequency of 40 Hz. The measurements were performed with the magnetic field oriented perpendicular to the film plane. This instrument allows for the measurements while sweeping the magnetic field continuously without pausing. Here, we used the slow rate of $dH/dt = 15$ Oe/s to avoid significantly out-of-equilibrium dynamic features. Figure 4 shows unusual peaklike features at intermediate magnetic fields compared to $H_{c2}(T)$, as shown in the lower-right inset. In the simplest approximation, there are two characteristic length scales that may result in such a peak when they match morphological features of the film of a characteristic length scale ℓ_p. These lengths are the coherence length, $\xi(T)$, and the intervortex distance, a. In our Nb films, the coherence length was estimated at $\xi(T) \approx 13$ nm [29] and is probably too small to produce such a matching feature, at least at low temperatures. This estimate agrees with other works; e.g., on a 180-nm-thick Nb film, it was found that $\xi(T) \approx 18.51$ nm [64]. The second length scale, $a(H)$, depends on a magnetic field and $M(H)$ will show a feature when $\ell_p \approx a(H)$ [65]. This defines the "matching field," H_{peak}. It is important to

note that if the pinning centers are arranged in the high-symmetry pattern, such as a square array of antidots on the $Mo_{0.79}Ge_{0.21}$ film, there are several matching fields that can be viewed as "harmonics" but the random distribution shows only one matching field corresponding to the mean distance between these pinning centers [65]. To account somehow for this randomness, we estimate a for the square- and triangular-vortex lattices. For the square-vortex lattice, $a = \sqrt{\phi_0/H_{\text{peak}}} \approx 45.473/\sqrt{H_{\text{peak}}}$ nm, where H_{peak} is in teslas. For the triangular-vortex lattice, $a = \sqrt{4\phi_0/\sqrt{3}H_{\text{peak}}} \approx 69.105/\sqrt{H_{\text{peak}}}$ nm. Figure 4(b) shows $a(T)$ evaluated from the data in Fig. 4(a). The green band in Fig. 4(b) shows a range of morphological features (grain sizes shown in Fig. 1) estimated to be between 30 and 90 nm. The intervortex distance, $a(T)$, is within this interval up to about 4 K. The overall temperature dependence of $H_{\text{peak}}(T)$ is shown in Fig. 4(c), along with $H_{c2}(T)$ for comparison. Clearly, this feature is not related to the upper critical field and represents the pinning properties of a fairly dilute vortex lattice. Whether or not this peak-effect phenomenon is common for particular niobium films needs to be studied separately on films of different thicknesses and, most importantly, with different grain sizes. For now, we can state that the intervortex distance matches characteristic morphological sizes determined from electron-microscopy imaging. We note that our films show a much larger magnetic hysteresis
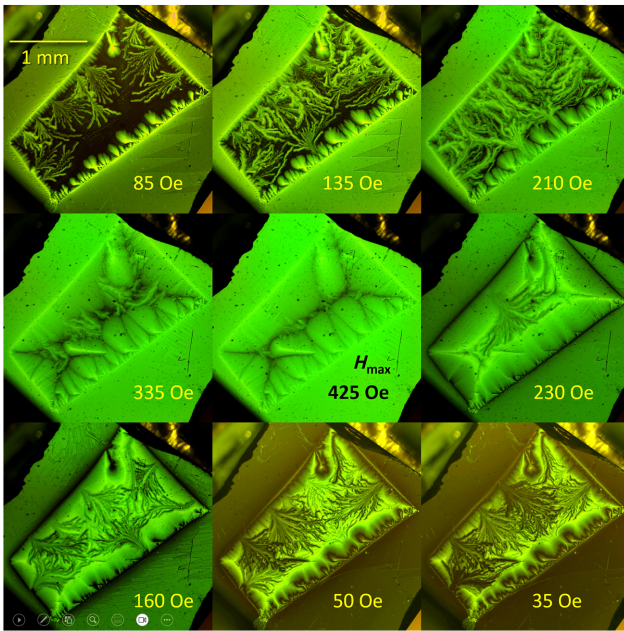
FIG. 5. Magneto-optical imaging of the magnetic induction in a thin-film sample at $T = 5$ K. The magnetic field was applied perpendicular to the film plane after cooling the sample in zero magnetic field. The first five images show flux penetration, $H = 85, 135, 210, 335,$ and 425 Oe. After that, the magnetic field was reduced, imaging the flux exit and trapping in the sample, $H = 230, 160, 50,$ and 35 Oe (the process is depicted in Videos 1 and 2). The scale bar is shown in the top-left image.

compared to the bulk samples and single crystals [56,66]. However, the very large demagnetizing factor of a thin film plays a significant role in the appearance of the $M(H)$ loops and such comparison should be made with caution [67–71].

We now examine the details of the magnetic flux penetration and exit using direct magneto-optical imaging of the superconducting state using specially fabricated transparent ferrimagnetic indicators placed on top of samples [51,72,73]. Figure 5 shows the sequence of images obtained after cooling in zero magnetic field to 5 K. The first five frames (left to right, top to bottom) show increasing magnetic field up to the maximum of $H_{max} = 425$ Oe, after which the magnetic field was reduced and flux was exiting the sample. There are two distinct regimes of flux penetration and exit. First, there are large-scale very fast dendritic avalanches (see Videos 1 and 2), similar in their appearance to lightning strikes. Similar behavior was observed long ago in various films, particularly niobium, and is well understood [28,74–81]. The physics behind it is straightforward. When first vortices are pushed inside by the screening currents, these moving vortices induce an electric field parallel to the currents, resulting in a resistive state, and energy is dissipated. If there is an insufficient thermal link to the surrounding and, in the case of films,
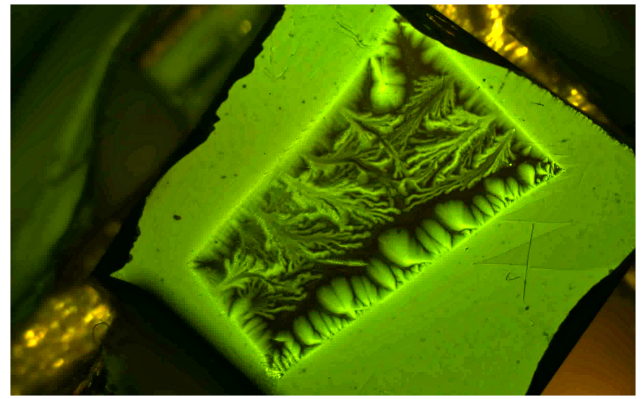
VIDEO 1. A real-time video of the magnetic flux penetration into a 160-nm-thick niobium film at $T = 5$ K. Figure 5 shows the snapshots from this video. Initially, flux enters as rapid bursts of thermomagnetic instabilities (avalanches) initiated at some weak spots at the film boundary. This is then followed by a more regular flux penetration, in agreement with the critical-state model, where the speed of front propagation is commensurate with the (slow) ramp rate of the applied magnetic field. After the maximum field is reached and the dendrites are wiped out, an external magnetic field is reduced and now new dendrites of the opposite sign appear, since the overall current density is reversed and vortices are exiting the sample. Importantly, dendrites are still initiated at the weak spots on sample edges as antiflux enters the sample and annihilates the flux inside.

to the substrate [75], the released heat decreases the local critical current in the direction of the vortex motion, creating a self-heating violent unidirectional propagation of bunches of vortices that follow the heated trail that needs time to dissipate via thermal diffusion. Sometimes they branch out when meeting various obstacles and, in this case, most likely the grain boundaries. In thicker samples (foils a few tens of micrometers thick), the avalanches may become "global," leading to a catastrophic collapse of the entire Bean critical state [73]. The actual local temperature instabilities have been measured during these processes. In the case of QIS applications, this insufficient heat channeling may represent a difficult problem. The second stage of flux penetration is a regular Bean-critical-state pattern [67,68,70], which is also somewhat nonuniform, following the granular film morphology. When the external magnetic field is decreased, the reverse process happens and similar dendritic avalanches start to channel out, now shown by a darker color corresponding to the local suppression of the magnetic induction. In the end, the mix of uniform and nonuniform trapped flux remains in the sample as a fingerprint of the intense perturbations occurring when the field was ramped up and down.

Real-time movies of the processes pictured in Fig. 5 are presented in Videos 1 and 2. This highly inhomogeneous magnetic flux evolution reveals the issues of thermal heat sinking and morphological inhomogeneity. Video 1
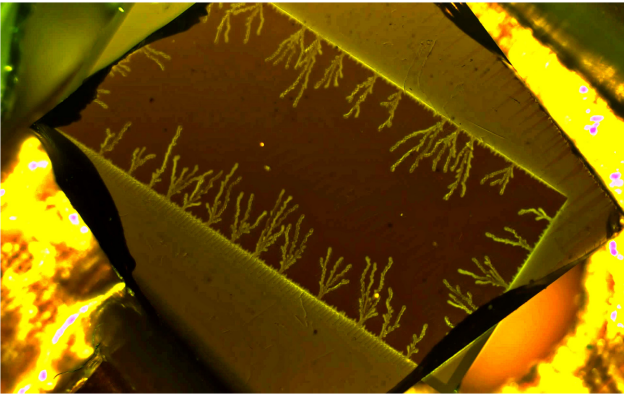
VIDEO 2. The magnetic field penetration was stopped at $H = 450$ Oe and the sample was slowly warmed up through T_c. The initially sharp dendrites start to become fuzzy due to annealing of the steepest slopes at the dendrite front. This indicates that the dendrites are completely static remnants of the rapidly propagated avalanches.

shows a real-time video of the magnetic flux penetration into a 160-nm-thick niobium film at $T = 5$ K, while Fig. 5 shows the snapshots from this video. Initially, magnetic flux enters as rapid bursts of thermomagnetic instabilities (avalanches) initiated at some weak spots at the film boundary. This is then followed by a more regular flux penetration, in agreement with the critical-state model, in which only the average persistent current density controls the average flux gradient. The speed of front propagation is commensurate with the (slow) ramp rate of the applied magnetic field (the video is in real time). Of course, locally, the flux gradient may exceed the average critical value and a small avalanche may be released. However, it does not lead to a large-scale discharge. The overall process maps onto a model of self-organized criticality discussed in detail elsewhere [82–84]. It leads to a power-law power spectrum of the avalanche statistics and has the direct impact of flux creep [83]. After the maximum field is reached and the dendrites are wiped out by uniform Bean fronts, an external magnetic field is reduced and now new dendrites of the opposite sign appear, since the overall current density is reversed and vortices are exiting the sample. Importantly, new dendrites are still initiated at the weak spots on sample edges as the antiflux enters the sample and annihilates the flux inside. This is purely due to the high demagnetizing factor of the thin-film sample in a perpendicular field. Video 2 shows the annealing of a highly nonuniform flux distribution created by the avalanches. Here, the external magnetic field was stopped at $H = 450$ Oe and the sample was slowly warmed up through T_c. The initially sharp highly branched-out dendrites start to become fuzzy, with small branches merging, due to the annealing of the steepest slopes at the dendrite front. This

indicates that the dendrites are completely static remnants of the rapidly propagated avalanches.

IV. DISCUSSION

Let us review the experimental findings and try to understand all the different results from a common point of view. All measurements indicate that as far as superconducting properties are concerned, the films are rather far from being ideal and exhibit various irreversible properties that generally lead to dissipation and hence quantum decoherence.

One of the most puzzling facts is that while $RRR = 5$ is rather very low, the superconducting transition temperature, $T_c = 9.35$ K, is as high as in good single crystals. According to the theory, T_c should be suppressed by nonmagnetic disorder due to anisotropy of the order parameter and the multiband nature of the material [58]. However, the same theory predicts the saturation of T_c when the gap averages out at higher scattering rates. Still, T_c should be lower than 9 K, and it is not. One natural way to understand this, supported by the direct electron-microscopy imaging [see Fig. 1], is to assume that grains themselves are quite clean in terms of the scattering rate but the random network of grain boundaries creates significant resistance. The boundaries do not, however, affect high T_c inside the grains. In the normal state, just above T_c, the resistivity is mostly determined by those boundaries. However, when the grains become superconducting, the boundaries become a network of Josephson junctions and the whole sample transitions to zero resistance. This explains the low RRR and, simultaneously, high T_c.

The heterogeneous granular structure also explains the measurements of the third and the upper critical fields, shown in Fig. 2. While it is important to measure these two fields in one experiment and on the same sample, the problem is that their ratio is about 1.3, whereas a ratio of at least 1.7 is expected theoretically, even in the dirty limit [59]. However, real sample-geometry and surface conditions may significantly affect the H_{c3} [49] beyond the pointlike scattering and smooth semi-infinite surface with the perfectly parallel field considered in Ref. [59]. Therefore, our granular film does not show the expected maximum value of this ratio. This is further reinforced by the clear matching effect at a length scale of around 50 nm [see Fig. 4], which correlates with the granular structure revealed by the film electron microscopy [see Fig. 1].

Finally, the thermomagnetic instabilities found in our study indicate an impeded heat flow and removal in these films. While QIS applications of thin films do not use an external magnetic field, the transmons are driven at high frequencies and show elevated dissipation due to morphological inhomogeneities. In particular, the granular structure may contribute to their additional distortion of the current flow and extra resistance [85,86]. Another

possible source is Kapitza resistance due to phonon-flow mismatch at the boundaries and the interfaces [86]. Finally, occasional vortices may enter the structure due to extreme demagnetization and sharp edges. With or without vortices, heat dissipation and cooling may become a serious issue if the device is located in a high vacuum and can only sink heat through a substrate.

On the other hand, the films show clean exponential attenuation of the weak magnetic field, signaling a fairly clean superconducting gap. Therefore, they still have potential for improvement and here we suggest some strategies.

A. Suggested mitigation strategies

A few suggestions can be made regarding the application of such films for superconducting qubits:

(1) To investigate the impeded heat transfer and dissipation, one may try to measure the coherence times and the quality factor by comparing the same transmon qubit in vacuum and via immersion in liquid ^{3}He, into a separate pot with liquid ^{3}He.

Interestingly, Lucas *et al.* [87] have recently reported on the immersion of a superconducting NbN-thin-film-based circuit in liquid ^{3}He pot cooled by an adiabatic demagnetization stage to temperatures less than 1 mK, which improved all QIS-relevant parameters. The noise was noticeably decreased starting from 80 mK. This helps to confirm our mitigation suggestion and we have used the results of this experimental work to improve our discussion of this radical strategy.

(2) Reducing the substrate thickness may help to improve heat sinking when transmons are in a vacuum.

(3) The most problematic aspect of these films is that their granular structure may be fixed by switching to a different deposition method. The alternative methods producing better Nb films have been known for some time [25,26]. For example, molecular-beam epitaxy (MBE) has been shown to produce Nb films of excellent crystallinity with $RRR \approx 200$ and, remarkably, $T_c = 9.45$ K [25]. In this case, different substrates and better-matching Nb thermal contraction and expansion, such as α-Al$_2$O$_3$ and MgO, were used.

(4) One may also try to perform postmanufacturing treatment of the prepared films, e.g., using recently introduced electroannealing, which has been used for the optimization of quantum interference devices [88].

(5) Finally, we have recently shown [29] that the introduction of true pointlike defects using proton irradiation expectedly reduces T_c somewhat, to around 9.16 K, which indicates that it affects the interior of the grains. However, it also inhibits thermomagnetic instabilities, perhaps

because pointlike defects introduce a multiscale random-pinning landscape that impedes fast vortex motion. Furthermore, uniformly distributed dilute pointlike defects may benefit the transmons for other reasons. For example, they may reduce (pin or saturate) the activity of TLSs and also prevent phase slips in the Josephson network of grain boundaries. These ideas require further studies involving artificial disorder.

V. CONCLUSIONS

In summary, a comprehensive characterization of 160-nm-thick Nb films on [001] Si substrate used in superconducting transmons is presented. Electron microscopy, transport, magnetization, the London penetration depth quasiparticle spectroscopy, and real-space magneto-optical images all show that while these films have an outstanding superconducting transition temperature of $T_c = 9.35$ K and a clean superconducting gap, their behavior in the magnetic field is complicated, exhibiting significantly irreversible behavior, and with insufficient heat conductance leading to thermomagnetic instabilities. These may present an issue for further improvement of transmon quantum coherence. Possible mitigation strategies are suggested and the techniques presented here may provide guidelines for comprehensive characterization that can be used to improve materials for superconducting quantum computing.

[1] M. Reagor, W. Pfaff, C. Axline, R. W. Heeres, N. Ofek, K. Sliwa, E. Holland, C. Wang, J. Blumoff, K. Chou, M. J. Hatridge, L. Frunzio, M. H. Devoret, L. Jiang, and R. J. Schoelkopf, Quantum memory with millisecond coherence in circuit QED, Phys. Rev. B **94**, 014506 (2016).

[2] M. Kjaergaard, M. E. Schwartz, J. Braumüller, P. Krantz, J. I.-J. Wang, S. Gustavsson, and W. D. Oliver, Superconducting qubits: Current state of play, Annu. Rev. Condens. Matter Phys. **11**, 369 (2020).

[3] M. S. Alam *et al.*, Quantum computing hardware for HEP algorithms and sensing (2022).

[4] P. Jurcevic *et al.*, Demonstration of quantum volume 64 on a superconducting quantum computing system, Quantum Sci. Technol. **6,** 025020 (2021).

[5] N. P. de Leon, K. M. Itoh, D. Kim, K. K. Mehta, T. E. Northup, H. Paik, B. S. Palmer, N. Samarth, S. Sangtawesin, and D. W. Steuerman, Materials challenges and opportunities for quantum computing hardware, Science **372,** eabb2823 (2021).

[6] S. Schlör, J. Lisenfeld, C. Müller, A. Bilmes, A. Schneider, D. P. Pappas, A. V. Ustinov, and M. Weides, Correlating Decoherence in Transmon Qubits: Low Frequency Noise by Single Fluctuators, Phys. Rev. Lett. **123,** 190502 (2019).

[7] J. Lee, Z. Sung, A. A. Murthy, M. Reagor, A. Grassellino, and A. Romanenko, Discovery of Nb hydride precipitates in superconducting qubits, arXiv:2108.10385 (2021).

[8] A. A. Murthy, J. Lee, C. Kopas, M. J. Reagor, A. P. McFadden, D. P. Pappas, M. Checchin, A. Grassellino, and A. Romanenko, TOF-SIMS analysis of decoherence sources in superconducting qubits, Appl. Phys. Lett. **120,** 044002 (2022).

[9] C. Müller, J. H. Cole, and J. Lisenfeld, Towards understanding two-level-systems in amorphous solids: Insights from quantum circuits, Rep. Prog. Phys. **82,** 124501 (2019).

[10] W. D. Oliver and P. B. Welander, Materials in superconducting quantum bits, MRS Bull. **38,** 816 (2013).

[11] C. Wang, C. Axline, Y. Y. Gao, T. Brecht, Y. Chu, L. Frunzio, M. H. Devoret, and R. J. Schoelkopf, Surface participation and dielectric loss in superconducting qubits, Appl. Phys. Lett. **107,** 162601 (2015).

[12] O. Dial, D. T. McClure, S. Poletto, G. A. Keefe, M. B. Rothwell, J. M. Gambetta, D. W. Abraham, J. M. Chow, and M. Steffen, Bulk and surface loss in superconducting transmon qubits, Supercond. Sci. Technol. **29,** 044001 (2016).

[13] J. M. Gambetta, C. E. Murray, Y. K. K. Fung, D. T. McClure, O. Dial, W. Shanks, J. W. Sleight, and M. Steffen, Investigating surface loss effects in superconducting transmon qubits, IEEE Trans. Appl. Supercond. **27,** 1 (2017).

[14] J. Burnett, L. Faoro, and T. Lindstrom, Analysis of high quality superconducting resonators: Consequences for TLS properties in amorphous oxides, Supercond. Sci. Technol. **29,** 044008 (2016).

[15] D. Niepce, J. J. Burnett, M. G. Latorre, and J. Bylander, Geometric scaling of two-level-system loss in superconducting resonators, Supercond. Sci. Technol. **33,** 025013 (2020).

[16] J. Verjauw, A. Potočnik, M. Mongillo, R. Acharya, F. Mohiyaddin, G. Simion, A. Pacco, T. Ivanov, D. Wan, A. Vanleenhove, L. Souriau, J. Jussot, A. Thiam, J. Swerts, X. Piao, S. Couet, M. Heyns, B. Govoreanu, and I. Radu, Investigation of Microwave Loss Induced by Oxide Regrowth in High-*Q* Niobium Resonators, Phys. Rev. Appl. **16,** 014018 (2021).

[17] A. Premkumar, C. Weiland, S. Hwang, B. Jaeck, A. Place, I. Waluyo, A. Hunt, V. Bisogni, J. Pelliciari, A. Barbour, M. Miller, P. Russo, F. Camino, K. Kisslinger, X. Tong, M. Hybertsen, A. Houck, and I. Jarrige, Microscopic relaxation channels in materials for superconducting qubits, Commun. Mater. **2,** 72 (2021).

[18] P. W. Anderson, Theory of dirty superconductors, J. Phys. Chem. Solids **11,** 26 (1959).

[19] M. Arai and T. Kita, *Ab initio* calculations of H_{c2} for Nb, $NbSe_2$, and MgB_2, J. Phys. Soc. Jpn. **73,** 2924 (2004).

[20] M. Bahte, F. Herrmann, and P. Schmuser, Magnetization and susceptibility measurements on niobium samples for cavity production, Part. Accel. **60,** 121 (1998).

[21] F. Barkov, A. Romanenko, Y. Trenikhina, and A. Grassellino, Precipitation of hydrides in high purity niobium after different treatments, J. Appl. Phys. **114,** 164904 (2013).

[22] F. Barkov, A. Romanenko, and A. Grassellino, Direct observation of hydrides formation in cavity-grade niobium, Phys. Rev. Spec. Top.—Accel. Beams **15,** 122001 (2012).

[23] P. Dhakal, G. Ciovati, and G. R. Myneni, Role of thermal resistance on the performance of superconducting radio frequency cavities, Phys. Rev. Accel. Beams **20,** 032003 (2017).

[24] A. M. Valente-Feliciano *et al.*, Next-generation superconducting rf technology based on advanced thin film technologies and innovative materials for accelerator enhanced performance and energy reach, arXiv:2204.02536 (2022).

[25] Gin-ichiro Oya, Masanori Koishi, and Yasuji Sawada, High-quality single-crystal Nb films and influences of substrates on the epitaxial growth, J. Appl. Phys. **60,** 1440 (1986).

[26] T. Wagner, High temperature epitaxial growth and structure of Nb films on alpha-Al_2O_3(0001), J. Mater. Res. **13,** 693 (1998).

[27] D. Bothner, T. Gaber, M. Kemmler, D. Koelle, and R. Kleiner, Improving the performance of superconducting microwave resonators in magnetic fields, Appl. Phys. Lett. **98,** 102504 (2011).

[28] F. Colauto, E. J. Patiño, M. G. Blamire, and W. A. Ortiz, Boundaries of the instability region on the *HT* diagram of Nb thin films, Supercond. Sci. Technol. **21,** 045018 (2008).

[29] M. A. Tanatar, D. Torsello, K. R. Joshi, S. Ghimire, C. J. Kopas, J. Marshall, J. Y. Mutus, G. Ghigo, M. Zarea, J. A. Sauls, and R. Prozorov, Anisotropic superconductivity of niobium based on its response to non-magnetic disorder, Phys. Rev. B **106,** 224511 (2022).

[30] K. M. Ryan, C. G. Torres-Castanedo, D. P. Goronzy, D. A. G. Wetten, M. Field, C. J. Kopas, J. Marshall, M. J. Reagor, M. J. Bedzyk, M. C. Hersam, and V. Chandrasekhar, Characterization of Nb films for superconducting qubits using phase boundary measurements, Appl. Phys. Lett. **121,** 202601 (2022).

[31] A. Nersisyan, S. Poletto, N. Alidoust, R. Manenti, R. Renzas, C.-V. Bui, K. Vu, T. Whyland, Y. Mohan, E. A. Sete, S. Stanwyck, A. Bestwick, and M. Reagor, Manufacturing low dissipation superconducting quantum processors, arXiv:1901.08042 (2019).

[32] A. A. Murthy, P. Masih Das, S. M. Ribet, C. Kopas, J. Lee, M. J. Reagor, L. Zhou, M. J. Kramer, M. C. Hersam, M. Checchin, A. Grassellino, R. d. Reis, V. P. Dravid, and A. Romanenko, Developing a chemical and structural understanding of the surface oxide in a niobium superconducting qubit, ACS Nano **16,** 17257 (2022).

[33] Jin-Su Oh, Xiaotian Fang, Tae-Hoon Kim, Matt Lynn, Matt Kramer, Mehdi Zarea, James A. Sauls, A. Romanenko, S. Posen, A. Grassellino, Cameron J. Kopas, Mark Field, Jayss Marshall, Hilal Cansizoglu, Joshua Y. Mutus, Matthew Reagor, and Lin Zhou, Multi-modal electron microscopy study on decoherence sources and their stability in Nb based superconducting qubit, arXiv:2204.06041 (2022).

[34] R. Lutchyn, L. Glazman, and A. Larkin, Quasiparticle decay rate of Josephson charge qubit oscillations, Phys. Rev. B **72**, 014517 (2005).

[35] I. Siddiqi, Engineering high-coherence superconducting qubits, Nat. Rev. Mater. **6**, 875 (2021).

[36] R. Prozorov and R. W. Giannetta, Magnetic penetration depth in unconventional superconductors, Supercond. Sci. Technol. **19**, R41 (2006).

[37] R. Prozorov and V. G. Kogan, London penetration depth in iron-based superconductors, Rep. Prog. Phys. **74**, 124505 (2011).

[38] R. Prozorov, M. Zarea, and J. A. Sauls, Niobium in the clean limit: An intrinsic type-I superconductor, Phys. Rev. B **106**, L180505 (2022).

[39] C. T. V. Degrift, Tunnel diode oscillator for 0.001 ppm measurements at low temperatures, Rev. Sci. Instrum. **46**, 599 (1975).

[40] R. Prozorov, R. W. Giannetta, A. Carrington, and F. M. Araujo-Moreira, Meissner-London state in superconductors of rectangular cross section in a perpendicular magnetic field, Phys. Rev. B **62**, 115 (2000).

[41] R. Prozorov, R. W. Giannetta, A. Carrington, P. Fournier, R. L. Greene, P. Guptasarma, D. G. Hinks, and A. R. Banks, Measurements of the absolute value of the penetration depth in high-T_c superconductors using a low-T_c superconductive coating, Appl. Phys. Lett. **77**, 4202 (2000).

[42] R. Prozorov, Meissner-London Susceptibility of Superconducting Right Circular Cylinders in an Axial Magnetic Field, Phys. Rev. Appl. **16**, 024014 (2021).

[43] W. N. Hardy, D. A. Bonn, D. C. Morgan, R. Liang, and K. Zhang, Precision Measurements of the Temperature Dependence of λ in YBa$_2$Cu$_3$O$_{6.95}$: Strong Evidence for Nodes in the Gap Function, Phys. Rev. Lett. **70**, 3999 (1993).

[44] J. D. Kokales, P. Fournier, L. V. Mercaldo, V. V. Talanov, R. L. Greene, and S. M. Anlage, Microwave Electrodynamics of Electron-Doped Cuprate Superconductors, Phys. Rev. Lett. **85**, 3696 (2000).

[45] W. A. Huttema, B. Morgan, P. J. Turner, W. N. Hardy, X. Zhou, D. A. Bonn, R. Liang, and D. M. Broun, Apparatus for high-resolution microwave spectroscopy in strong magnetic fields, Rev. Sci. Instrum. **77**, 023901 (2006).

[46] S. Bae, Y. Tan, A. P. Zhuravel, L. Zhang, S. Zeng, Y. Liu, T. A. Lograsso, Ariando, T. Venkatesan, and S. M. Anlage, Dielectric resonator method for determining gap symmetry of superconductors through anisotropic nonlinear Meissner effect, Rev. Sci. Instrum. **90**, 043901 (2019).

[47] D. H. Wu, J. Mao, S. N. Mao, J. L. Peng, X. X. Xi, T. Venkatesan, R. L. Greene, and S. M. Anlage, Temperature Dependence of Penetration Depth and Surface Resistance of Nd$_{1.85}$Ce$_{0.15}$CuO$_4$, Phys. Rev. Lett. **70**, 85 (1993).

[48] A. A. Abrikosov, *Fundamentals of the Theory of Metals* (Dover Publications, Newburyport, Massachusetts, 2017).

[49] V. G. Kogan, J. R. Clem, J. M. Deang, and M. D. Gunzburger, Nucleation of superconductivity in finite anisotropic superconductors and the evolution of surface superconductivity toward the bulk mixed state, Phys. Rev. B **65**, 094514 (2002).

[50] Y. Liu, M. A. Tanatar, V. G. Kogan, H. Kim, T. A. Lograsso, and R. Prozorov, Upper critical field of high-quality single crystals of KFe$_2$As$_2$, Phys. Rev. B **87**, 134513 (2013).

[51] M. V. Indenbom, T. Schuster, M. R. Koblischka, A. Forkl, H. Kronmueller, L. A. Dorosinskii, V. K. Vlasko-Vlasov, A. A. Polyanskii, R. L. Prozorov, and V. I. Nikitenko, Study of flux distributions in high-T_c single crystals and thin films using magnetooptic techniques, Physica C **209**, 259 (1993).

[52] R. Prozorov, R. W. Giannetta, A. A. Polyanskii, and G. K. Perkins, Topological hysteresis in the intermediate state of type-I superconductors, Phys. Rev. B **72**, 212508 (2005).

[53] R. Prozorov, Equilibrium Topology of the Intermediate State in Type-I Superconductors of Different Shapes, Phys. Rev. Lett. **98**, 257001 (2007).

[54] R. Prozorov, A. Fidler, J. Hoberg, and P. Canfield, Suprafroth in type I superconductors, Nat. Phys. **4**, 327 (2008).

[55] D. B. Liarte, S. Posen, M. K. Transtrum, G. Catelani, M. Liepe, and J. P. Sethna, Theoretical estimates of maximum fields in superconducting resonant radio frequency cavities: Stability theory, disorder, and laminates, Supercond. Sci. Technol. **30**, 033002 (2017).

[56] D. K. Finnemore, T. F. Stromberg, and C. A. Swenson, Superconducting properties of high-purity niobium, Phys. Rev. **149**, 231 (1966).

[57] E. M. Lechner, B. D. Oli, J. Makita, G. Ciovati, A. Gurevich, and M. Iavarone, Electron Tunneling and X-Ray Photoelectron Spectroscopy Studies of the Superconducting Properties of Nitrogen-Doped Niobium Resonator Cavities, Phys. Rev. Appl. **13**, 044044 (2020).

[58] M. Zarea, H. Ueki, and J. A. Sauls, Effects of anisotropy and disorder on the superconducting properties of niobium, arXiv:2201.07403 (2022).

[59] H.-Y. Xie, V. G. Kogan, M. Khodas, and A. Levchenko, Onset of surface superconductivity beyond the Saint-James–de Gennes limit, Phys. Rev. B **96**, 104516 (2017).

[60] A. Koethe and J. I. Moench, Preparation of ultra high purity niobium, Mater. Trans., JIM **41**, 7 (2000).

[61] J. Bardeen, L. N. Cooper, and J. R. Schrieffer, Microscopic theory of superconductivity, Phys. Rev. **106**, 162 (1957).

[62] A. A. Abrikosov and L. P. Gor'kov, Contribution to the theory of superconducting alloys with paramagnetic impurities, Zh. Eksp. Teor. Fiz. (Sov. Phys. JETP 12, 1243 (1961)) **39**, 1781 (1960).

[63] V. Kogan, R. Prozorov, and V. Mishra, London penetration depth and pair breaking, Phys. Rev. B **88**, 224508 (2013).

[64] M. I. Valerio-Cuadros, D. A. D. Chaves, F. Colauto, A. A. M. de Oliveira, A. M. H. de Andrade, T. H. Johansen, W. A. Ortiz, and M. Motta, Superconducting properties and electron scattering mechanisms in a Nb film with a single weak-link excavated by focused ion beam, Materials **14**, 7274 (2021).

[65] Y. L. Wang, L. R. Thoutam, Z. L. Xiao, B. Shen, J. E. Pearson, R. Divan, L. E. Ocola, G. W. Crabtree, and W.

K. Kwok, Enhancing superconducting critical current by randomness, Phys. Rev. B **93,** 045111 (2016).

[66] T. F. Stromberg, Ph.D. thesis, Iowa State University, 1965.

[67] C. P. Bean, Magnetization of Hard Superconductors, Phys. Rev. Lett. **8,** 250 (1962).

[68] C. P. Bean, Magnetization of high-field superconductors, Rev. Mod. Phys. **36,** 31 (1964).

[69] E. H. Brandt, The flux-line lattice in superconductors, Rep. Prog. Phys. **58,** 1465 (1995).

[70] E. H. Brandt, Superconductor disks and cylinders in an axial magnetic field. I. Flux penetration and magnetization curves, Phys. Rev. B—Condens. Matter Mater. Phys. **58,** 6506 (1998).

[71] E. H. Brandt, Superconductors of finite thickness in a perpendicular magnetic field: Strips and slabs, Phys. Rev. B **54,** 4246 (1996).

[72] D. P. Young, M. Moldovan, P. W. Adams, and R. Prozorov, Magneto-optical studies of flux penetration in super-hard Nb wire, Supercond. Sci. Technol. **18,** 776 (2005).

[73] R. Prozorov, D. V. Shantsev, and R. G. Mints, Collapse of the critical state in superconducting niobium, Phys. Rev. B **74,** 220511 (2006).

[74] M. Motta, F. Colauto, W. A. Ortiz, J. Fritzsche, J. Cuppens, W. Gillijns, V. V. Moshchalkov, T. H. Johansen, A. Sanchez, and A. V. Silhanek, Enhanced pinning in superconducting thin films with graded pinning landscapes, Appl. Phys. Lett. **102,** 212601 (2013).

[75] E. Baruch-El, M. Baziljevich, T. H. Johansen, and Y. Yeshurun, Substrate influence on dendritic flux instability in YBCO thin films, J. Supercond. Novel Magn. **28,** 379 (2014).

[76] Z. Jing, H. Yong, and Y.-H. Zhou, Dendritic flux avalanches and the accompanied thermal strain in type-II superconducting films: Effect of magnetic field ramp rate, Supercond. Sci. Technol. **28,** 075012 (2015).

[77] E. Baruch-El, M. Baziljevich, B. Y. Shapiro, T. H. Johansen, A. Shaulov, and Y. Yeshurun, Dendritic flux instabilities in YBa$_2$Cu$_3$O$_{7-x}$ films: Effects of temperature and magnetic field ramp rate, Phys. Rev. B **94,** 054509 (2016).

[78] E. Baruch-El, M. Baziljevich, T. H. Johansen, X. Y. Zhou, X. Q. Jia, B. B. Jin, A. Shaulov, and Y. Yeshurun, Magnetic flux instability in NbN films exposed to fast field sweep rates, Supercond. Sci. Technol. **31,** 105008 (2018).

[79] S. Blanco Alvarez, J. Brisbois, S. Melinte, R. B. G. Kramer, and A. V. Silhanek, Statistics of thermomagnetic breakdown in Nb superconducting films, Sci. Rep. **9,** 3659 (2019).

[80] J. I. Vestgården, T. H. Johansen, and Y. M. Galperin, Nucleation and propagation of thermomagnetic avalanches in thin-film superconductors (review article), Low Temp. Phys. **44,** 460 (2018).

[81] F. Colauto, M. Motta, and W. A. Ortiz, Controlling magnetic flux penetration in low-T_C superconducting films and hybrids, Supercond. Sci. Technol. **34,** 013002 (2020).

[82] P. Bak, C. Tang, and K. Wiesenfeld, Self-organized criticality, Phys. Rev. A **38,** 364 (1988).

[83] R. Prozorov and D. Giller, Self-organization of vortices in type-II superconductors during magnetic relaxation, Phys. Rev. B **59,** 14687 (1999).

[84] R. J. Wijngaarden, M. S. Welling, C. M. Aegerter, and M. Menghini, Avalanches and self-organized criticality in superconductors, Eur. Phys. J. B—Condensed Matter and Complex Systems **50,** 117 (2006).

[85] A. Ramiere, C. Z. Antoine, and J. Amrit, Model for hot spots and Q-slope behavior in granular niobium thin film superconducting rf cavities, Phys. Rev. Accel. Beams **25,** 022001 (2022)

[86] K. Mizuno and T. Aomine, Current induced hotspot in superconducting thin films with different thicknesses, J. Phys. Soc. Jpn. **53,** 1434 (1984).

[87] M. Lucas, A. V. Danilov, L. V. Levitin, A. Jayaraman, A. J. Casey, L. Faoro, A. Y. Tzalenchuk, S. E. Kubatkin, J. Saunders, and S. E. de Graaf, Quantum bath suppression in a superconducting circuit by immersion cooling, Nat. Commun. **14,** 3522 (2023).

[88] S. Collienne, B. Raes, W. Keijers, J. Linek, D. Koelle, R. Kleiner, R. B. Kramer, J. Van de Vondel, and A. V. Silhanek, Nb-Based Nanoscale Superconducting Quantum Interference Devices Tuned by Electroannealing, Phys. Rev. Appl. **15,** 034016 (2021).